PEER-REVIEWED PAPER

Severe Plastic Deformed Zones and White Etching Layers Formed During Service of Railway Wheels

M. Freisinger[1,2] · H. Rojacz[1] · A. Trausmuth[1] · P. H. Mayrhofer[2]

Abstract

The near-surface regions of rail wheels experience a complex thermo-mechanical loading, which varies along the location of the tread and causes severe changes to the microstructure. Occasionally, brittle white etching layers (WEL) are formed, representing a high risk of wheel damage. Therefore, we studied the depth-evolution of the surface-near microstructure along different regions of the tread of a wheel being ~ 200,000 km in service. The microstructural variations point toward a higher thermal loading history in the middle of the tread and predominant mechanical loading in the neighboring regions, where a severe plastic deformed microstructure with rolling contact fatigue cracks is present. Varieties of WEL-like microstructures were investigated, the presented analysis contributes to the knowledge of their microstructural characteristics and outpoints these regions in terms of potential crack initiation sites on railway wheels.

Introduction

Medium carbon steels are commonly used for railway wheels due to a good balance of hardness and fracture toughness, as well as solid wear properties. Among rail wheel steels, the grade ER7 is one of the most used grades on freight trains in Europe. During service, the contact surface is affected by a complex mechanical loading situation in terms of vertical, tangential, and longitudinal loads [1]. High shear stresses can cause rolling contact fatigue (RCF) damage [2–5], and cracks propagating into the material can lead to catastrophic failure [6]. Besides the mechanical loads, the wheel tread surface is additionally affected by high thermal loads due to frictional heating during curving, braking, short slippage events when acceleration, or even occasional full slippage events. Temperatures can exceed 500 °C in slip zones on wheel tread surfaces [7] leading to a massive influence on microstructure and mechanical properties [8,

9]. Even though modern trains are equipped with wheel slide protection systems [10, 11] thermally induced damage is still an issue [10, 12, 13]. Additionally important are mechanical loads, which in combination with temperature heavily affect the near-surface microstructure [9, 14–16]. Besides the loading history, the microstructural evolution also varies on the location along the wheel tread surface [17, 18].

The formation of a white etching layer (WEL) can initiate cracks and promote their propagation [19–27], since the evolved microstructure of the WEL comes up with higher hardness and lower fracture toughness. Most studies are performed for railheads, but the comparable materials and rolling-sliding contact situation may allow transferring the gained know-how about the relevant mechanisms to railway wheels as well. The formation process is still under discussion, some studies predict heating above austenitization temperature followed by rapid cooling [21, 22, 25, 28] is the major cause, while others claim heavy plastic deformation [23, 24, 29], and further ones their combination [30, 31]. However, WEL can form in several variations–a common and consistent classification is still missing–on railway wheel tread surfaces [13, 32–34]. Recently, the terms brown etching layer (BEL) and stratified surface layer (SSL) are introduced [35–38], outpointing the diversity of the evolved microstructures.

✉ M. Freisinger
matthias.freisinger@ac2t.at

1   AC2T research GmbH, 2700 Wiener Neustadt, Austria

2   Institute of Materials Science and Technology, TU Wien, 1060 Vienna, Austria

The different variations are further summarized as WEL-like microstructures within this work.

The aim of this study is to study the evolved microstructure on railway wheels in greater detail, since this is the initial microstructural state before a possible formation of WEL-like microstructures (WEL, BEL, SSL). For this, the three main zones along a railway wheel tread after service are investigated. We concentrated on the microstructural evolution in transversal and rolling directions–in different depths from the surface–using light optical microscopy (LOM) as well as high magnification scanning electron microscopy (SEM) and electron backscatter diffraction (EBSD) measurements. Our studies also reveal different variations of WEL-like microstructures, characterized by different microstructures and hardness.

Experimental

A railway wheel of the wheel steel grade ER7 (EN13262 [39]) with a diameter of 0.95 m and after nearly 200,000 km in service was provided by the Austrian Federal Railways. Table 1 summarizes the chemical composition of this material, which typically shows an upper yield strength of $R_{eH} \geq 520$ MPa, a tensile strength R_m between 820 and 940 MPa, and an elongation at break A_5 of $\geq 14\%$. Brinell hardness is above 235 HB and a fracture toughness between 40 and 80 MPa m$^{1/2}$ is standardized [40], when treated and tested according to EN13262.

The samples for our investigations were prepared with a laboratory cutting device (Struers Secotom-50; Struers ApS, Denmark) out of three different zones of the railway wheel. These zones are named according to [41] as zone 1 (being taken from the peripheral tread region, at the field side), zone 2 (taken from the tread surface close to the wheel flange), and the middle zone 3 (major wheel tread) (Fig. 1a).

For each zone, multiple cross sections in transversal direction (CS-TD) and in rolling direction (CS-RD) are analyzed (Fig. 1b).

Samples taken from these zones are embedded in conductive compounds and prepared by coarse grinding, 1 μm diamond fine polishing, and etching with ethanolic nitric acid (3% HNO3, 97% ethanol). The microstructure is studied LOM (Axio Imager M2m, Carl Zeiss AG, Germany) and SEM (Jeol JIB 4700F, Jeol Ltd., Japan) equipped with a Schottky field emission gun, secondary and backscattered electron detectors, and an electron backscatter diffraction (EBSD) detector (Bruker e-Flash HR, USA). SEM investigations were performed at 15 kV acceleration voltage. To gain optimal results at the EBSD measurements, additional finish polishing for 10 min with colloidal Silica (< 0.25 μm) was carried out. EBSD measurements were performed in the SEM with optimized electron beam conditions at 15 kV acceleration voltage and a probe current of 3.6 nA. The working distance of the SEM was set to 16 mm, and the EBSD detector distance to 18 mm. Kikuchi patterns were acquired at 200×150 px with an exposure time of 20 ms. Setup and analysis were performed via the Bruker Esprit 2.2 software package, whereas the American Mineralogist Crystal Structure Database (AMCSD) database was used for phase identification. The inverse pole figure (IPF) maps, the grain average misorientation (GAM) maps, and the grain boundaries (GB) maps are presented in this work to describe the evolved microstructure in more detail. The IPF map is used to describe the grain structure in general, possible preferred orientations, and the grain size distribution. The GAM maps show the calculated misorientation between each neighboring pair of points within the grain and therefore give information about the orientation changes inside the grains. The GB maps are useful to evaluate the fraction of small angle grain boundaries, defined in this study with GB angles up to 10°, and large angle grain boundaries ($> 10°$).

Table 1 Maximum percentages of elements for ER7 according to the standard EN13262 [39]

C	Si	Mn	P	S	Cr	Cu	Mo	Ni	V
				[wt.%]					
0.52	0.40	0.80	0.020	0.015	0.30	0.30	0.08	0.30	0.06

Fig. 1 (**a**) Designated zones along the tread surface of the ER7 railway wheel after ~200,000 km in service. (**b**) Schematic illustration of the cross sections prepared in transversal direction (CS-TD) and rolling direction (CS-RD)
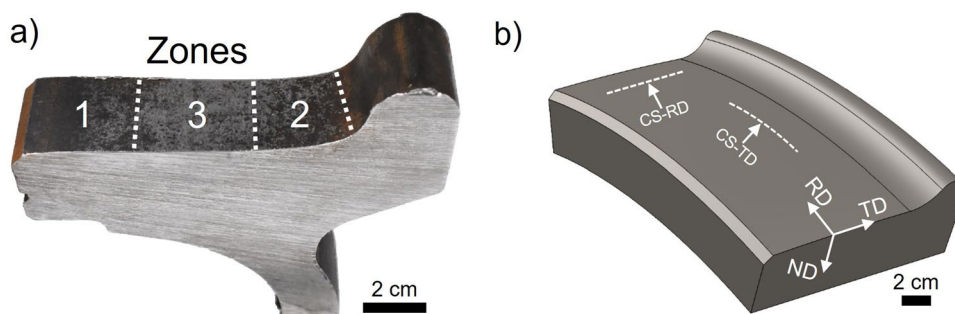
Hardness was investigated by low load Vickers hardness depth profiles (load of 0.05 kp (0.49 N)) indenting the cross sections at increasing distances from the surface with a Future-Tech FM-700 hardness tester. The diagonals of the indents are measured with a LOM. Furthermore, nanoindentation measurements of individual regions within the samples were performed with a Bruker Hysitron Triboindenter TI980–Performech II (equipped with a Berkovich diamond tip) to characterize their indentation hardness as well as moduli. The load–displacement curves (with a peak load of 5 mN) were evaluated and the hardness was deduced via the load/area ratio, whereby the reduced Young's modulus was evaluated via the Oliver and Pharr method [42].

Results

Out of each zone, several cross sections in transversal direction and rolling direction were prepared and analyzed. The presented images indicate that there is no preferred rolling direction, this is because this study is based on a railway wheel from the field where the running direction was changing over the service.

### Characteristic Microstructural Evolution in Different Wheel Tread Zones

In the peripheral tread region (field side) of the wheel, zone 1, the cross section CS-TD (Fig. 2a) shows numerous cracks with depths of ~ 100 μm propagating in a severely plastically deformed (SPD) microstructure, which expands down to ~ 300 μm from the surface. Some of the cracks are wide opened and/or changing crack growth direction leading to multiple spalling of the material, hence, resulting in a rough surface. In a depth of 300–600 μm from the surface the microstructure gradually changes from a fine-grained SPD microstructure with random orientation to a ferritic-pearlitic microstructure (with elongated grains in rolling direction, aligned with about 30–45° to the surface). The elongation, alignment, and grain size decrease with increasing distance from the surface, featuring a ferritic-pearlitic bulk microstructure without preferred orientation upon ~ 600 μm from surface.

For the cross section CS-RD in zone 1 (Fig. 2b) a rough surface can be seen as described for CS-TD due to numerous spallation. But this cross section in rolling direction additionally shows long cracks propagating almost parallel to the tread surface in depths of about 100 μm. These cracks are branching or merging at certain stages, which leads to large spallation. The evolution of the sub-surface microstructure is in general comparable to that shown for the cross section CS-TD: A gradual change from a fine-grained and randomly orientated SPD microstructure at ~ 300 μm from surface to a ferritic-pearlitic microstructure. The latter is aligned parallel to the surface with increasing grain size from 300 to 600 μm with increasing distance from the surface. At ≥ 600 μm below the surface, the original bulk microstructure is present.

In the middle of the wheel tread, designated as zone 3, the cross section CS-TD (Fig. 2c) shows that the fine-grained microstructure reaches deeper into the material than for zone 1, although, the depth is varying widely between 300 and 700 μm from the surface. Below that

Fig. 2 Sub-surface microstructure LOM images of the ER7 railway wheel after ~ 200,000 km in service. The first column shows the cross-ections in zone 1: (**a**) in transversal direction (CS-TD) and (**b**) in rolling direction (CS-RD). The second column shows the middle zone 3: (**c**) CS-TD and (**d**) CS-RD, and the third column the zone 2: (**e**) CS-TD, (**f**) CS-RD
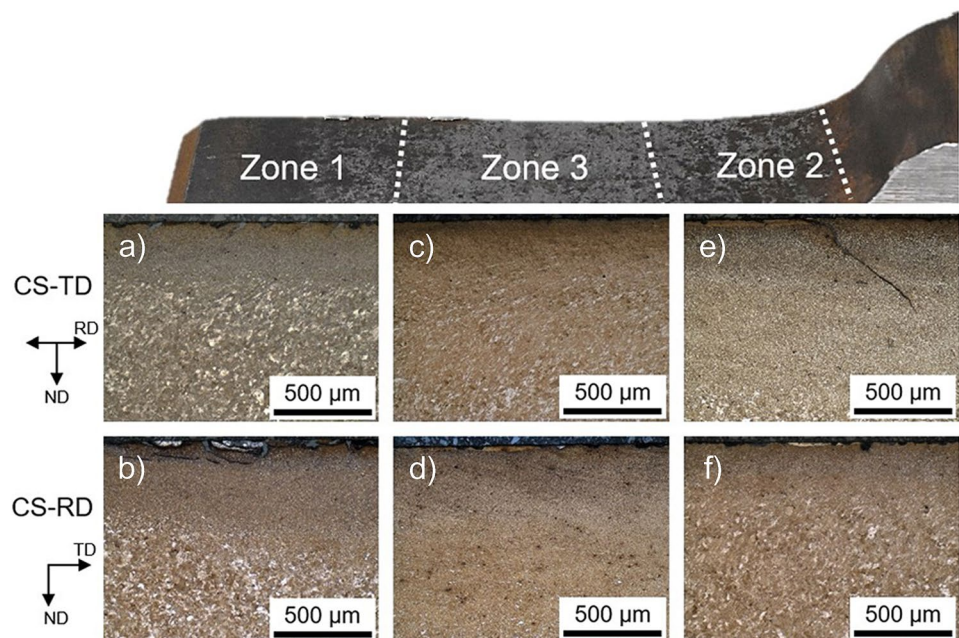
region, the microstructure changes gradually to an aligned SPD microstructure with decreasing deformation degree with increasing depth. Within zone 3, the thickness of the influenced microstructure varies widely within a maximum of ~ 1,000 μm. Also in rolling direction, the microstructure is comparable (Fig. 2d). Here, a formation of a thin WEL can be detected with a thickness of about 30 μm.

The cross-sectional LOM image of the region close to the wheel flange (zone 2, Fig. 2e) clearly shows massive cracks, which mainly originate from regions where a WEL is present. These cracks typically propagate down to depths of ~ 600 μm with an angle of about 45° from surface. Some cracks branch within the WEL and/or grow along the interface between WEL and underlying material, leading to spallation. A fine-grained microstructure is present down to almost 900 μm from surface. Below this uniform microstructure, there is immediately the original microstructure.

Microstructural investigations of the material in rolling direction (Fig. 2f) exhibit similar features as perpendicular to it. Below the fine-grained microstructure, there is directly the original microstructure, without the presence of an aligned SPD microstructure as within the other two zones.

Detailed investigations of zone 1 (Fig. 2a) by higher magnification SEM and EBSD measurements on cross sections perpendicular to the rolling direction in different depths from the surface are presented in Fig. 3. At a depth of 50 μm (Fig. 3a) a fragmentation (and possible dissolution) of the cementite is evident and the spherical cementite particles are randomly distributed. At a depth of 100 μm (Fig. 3b) and 150 μm (Fig. 3c) the microstructural features are comparable, with a slightly less dense arrangement. For the regions at distances of ~ 150 μm (Fig. 3c), 300 μm (Fig. 3d), 600 μm (Fig. 3e), and 1500 μm (Fig. 3f) below the surface detailed EBSD measurements were conducted and evaluated for their IPFs, GAM, GBs. The IPF map for the region at ~ 150 μm from the surface shows a fine-grained microstructure with slightly elongated grains and no preferred orientation. The fraction of large angle grain boundaries (with misorientation angles between adjacent grains of ≥ 10°) is relatively high (Fig. 3c). At a depth of 300 μm, the SEM investigations suggest for larger grains (Fig. 3d), bent and broken cementite lamellae (next to spheroidized particles), and proeutectoid ferrite. EBSD investigations of this region prove the larger grains, which seem to be elongated along the rolling direction (Fig. 3h). The GAM map analysis shows a wider GAM angle distribution than the region closer to the surface.

At a depth of 600 μm from the surface, the microstructure is comparable to the original condition with clearly present pearlite and ferrite grains (Fig. 3e). The original microstructure is essentially present at a distance of 1500 μm from the surface (Fig. 3f). The GAM analysis of the EBSD measurements (Fig. 3i) show that the highest misorientation angles are at the lamellar structures of pearlite, and the respective GB analysis yield only a fraction of 25–18% of small angle GB (angle below 10°).

Detailed analysis of zone 3 (Fig. 2c) by SEM (Fig. 4) show spheroidized cementite (Fig. 4a) down to 100 μm (Fig. 4b) and even 150 μm from the surface (Fig. 4c). With increasing distance from the surface, the overall microstructure gradually changes toward the original one (Fig. 4d, e, and f). EBSD analyzes of the region 150 μm below the surface (Fig. 4g) show a fine-grained microstructure with slightly elongated grains. The GAM angle map pictures low misorientation angles and the fraction of large angle grain boundaries (angles > 10°) is high with ~ 86%. At a distance of 300 μm from the surface (Fig. 4h), the microstructure is still very similar with slightly more pronounced elongated grains (represented by the IPF map) and a smaller fraction of large angle grain boundaries.

With further distance from the surface, (300 μm, Fig. 4d) the fraction of spheroidized cementite decreases and that of cementite lamellae increases, suggesting less broken and annealed cementite lamellae upon this depth. However, even at 600 μm from the surface (Fig. 4e), spheroidized particles are present. The corresponding IPF map (Fig. 4i) shows a mixture of elongated grains (orientated in rolling direction) and polygonal grains. At this distance from the surface there are more areas with larger GAM angles than closer to the surface and the fraction of small angle grain boundaries (< 10° misorientation) increased to almost 17%. Contrary to zone 1, here, even at a depth of 1500 μm (Fig. 4f), broken and bent cementite lamellae are present within the pearlite grains. Further, the EBSD investigations do not represent an unaffected bulk microstructure like in zone 1 at this depth. Clearly, a sub-grain microstructure is present.

Detailed SEM investigations of zone 2 (Fig. 2e), 50 μm below the surface perpendicular to the rolling direction, show fine globular particles (Fig. 5a). Although generally, the overall microstructure is similar to that of zone 1 and zone 3 at this depth (compare with Fig. 3 and Fig. 4), still some cementite lamellae are present here. At distances of 100 μm (Fig. 5b) and 150 μm (Fig. 5c) from the surface, the overall microstructure is very similar to that at 50 μm, with tendencies of an increased fraction of cementite lamellar. This tendency continues with increasing distance from the surface (300 μm, Fig. 5d), and at a distance of 600 μm (Fig. 5e) the grains are already more globular with cementite lamellae fragments and proeutectoid ferrite. At a distance of 1500 μm the original pearlitic microstructure is present (Fig. 5f).

EBSD measurements clearly show elongated grains aligned parallel to the rolling direction at a distance of 150 μm from the surface (Fig. 5g). Compared with the other zones, the grain size is larger. With increasing distance (Fig. 5h and i), the grain size further increases while
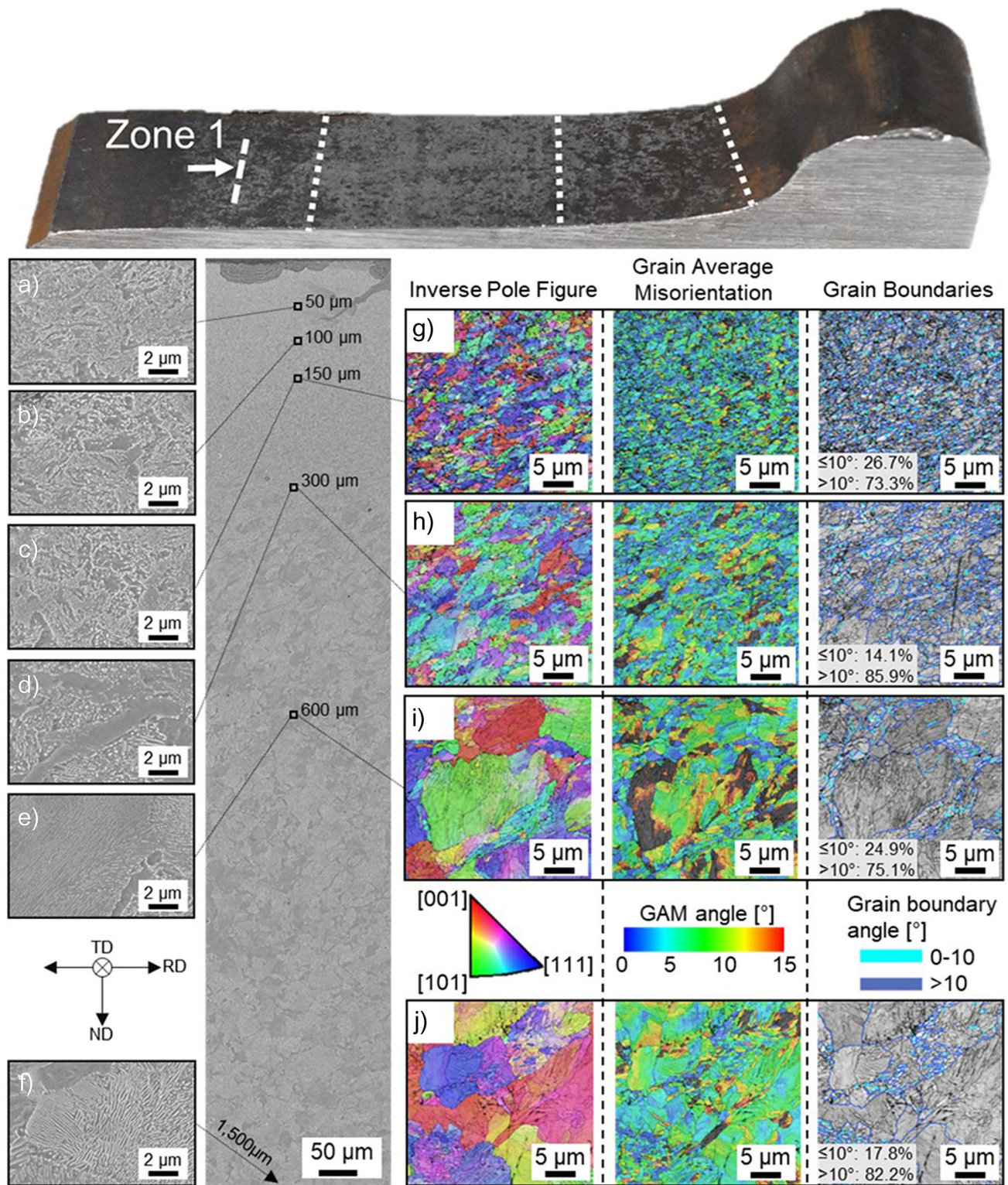
Fig. 3 Detailed SEM investigations of the zone 1 in transversal direction (CS-TD): Micrographs with a magnification of 35,000× are presented in various depths in the first column: (a) 50 μm, (b) 100 μm, (c) 150 μm, (d) 300 μm, (e) 600 μm, and (f) 1500 μm. Inverse pole figure, grain average misorientation and grain boundary maps from EBSD measurements are shown for selected depths on the right side: (g) 150 μm, (h) 300 μm, (i) 600 μm, and (j) 1500 μm
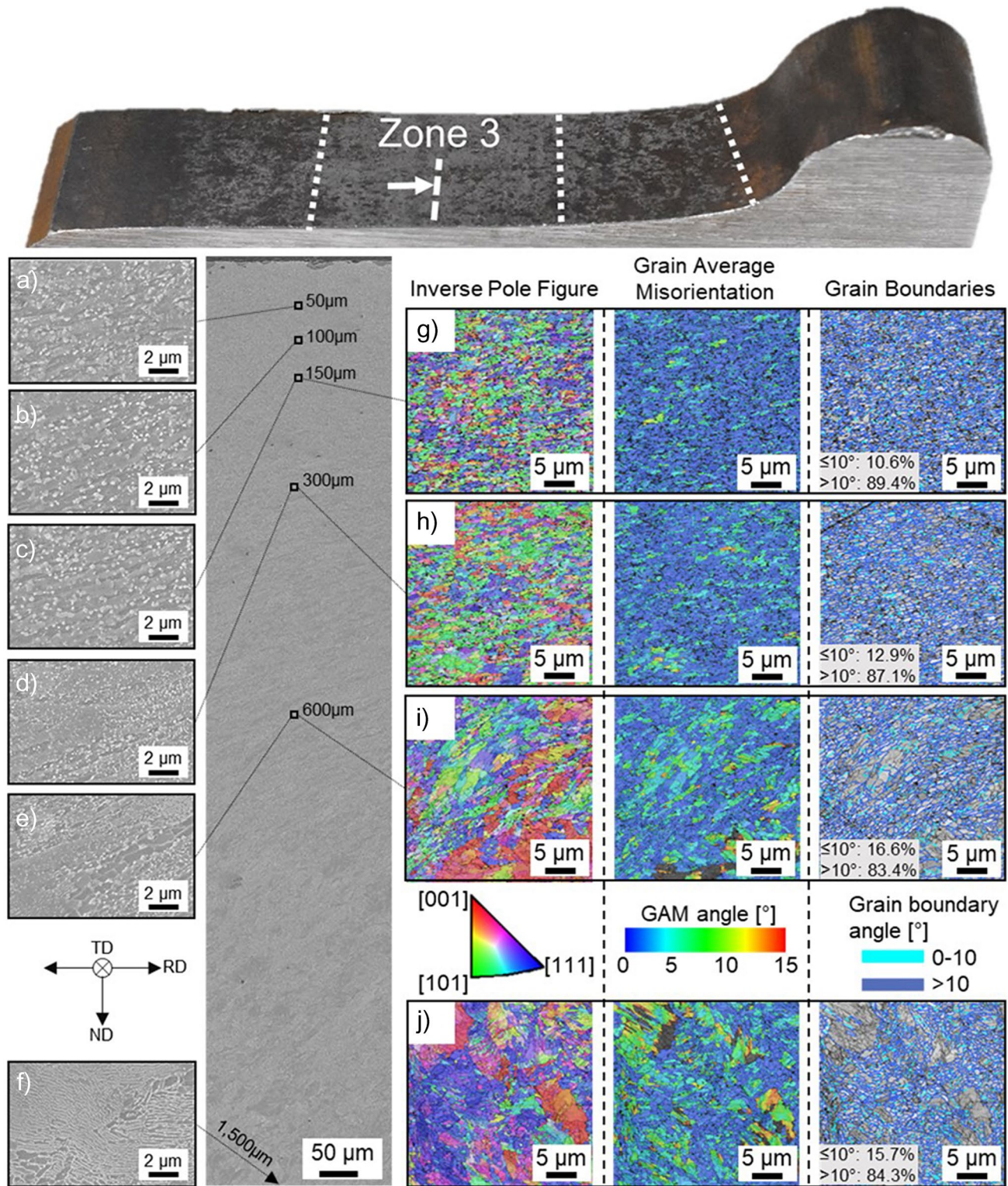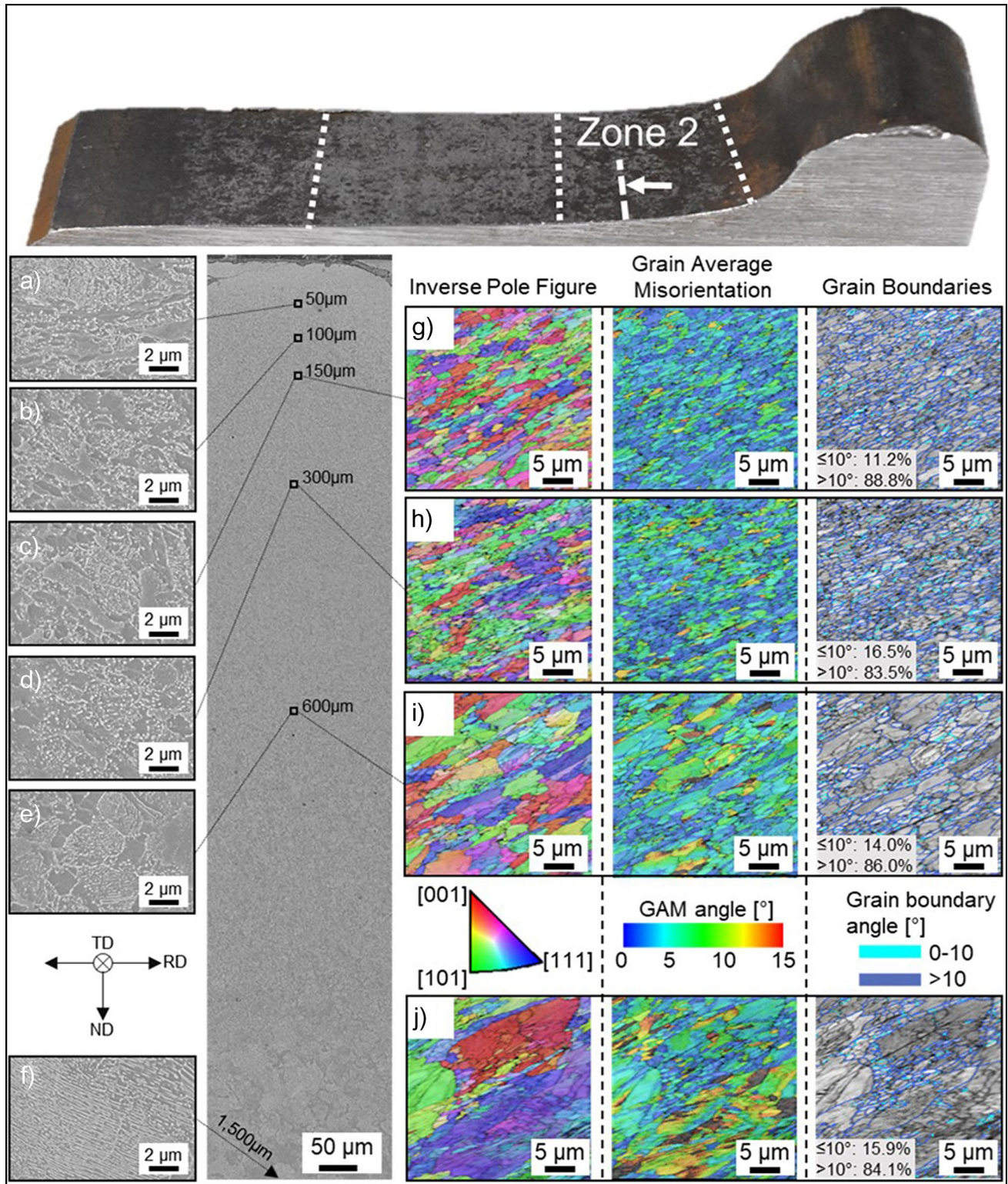
Fig. 4 Detailed SEM investigations of the zone 3 in transversal direction (CS-TD): Micrographs with a magnification of 35,000× are presented in various depths in the first column: (**a**) 50 μm, (**b**) 100 μm, (**c**) 150 μm, (**d**) 300 μm, (**e**) 600 μm, and (**f**) 1500 μm. Inverse pole figure, grain average misorientation and grain boundaries maps from EBSD measurements are shown for selected depths on the right side: (**g**) 150 μm, (**h**) 300 μm, (**i**) 600 μm, and (**j**) 1500 μm

Fig. 5 Detailed SEM investigations of the zone 2 in transversal direction (CS-TD): Micrographs with a magnification of 35,000× are presented for various distances from the surface: (**a**) 50 μm, (**b**) 100 μm, (**c**) 150 μm, (**d**) 300 μm, (**e**) 600 μm, and (**f**) 1500 μm. Inverse pole figure, grain average misorientation, and grain boundary maps from EBSD measurements are shown for (**g**) 150 μm, (**h**) 300 μm, (**i**) 600 μm, and (**j**) 1500 μm distances from the surface

still being aligned in rolling direction. Areas with larger GAM angles increase and the fraction of large angle grain boundaries decreases. Even at a distance of 1500 μm from the surface, the EBSD investigations (Fig. 5j) hint toward a modified microstructure with elongated ferrite and pearlite grains aligned in rolling direction.

Microhardness is determined by Vickers hardness measurements, the results show an increase within 200 μm from surface for zone 1 and zone 2, in contrast to no significant change in zone 3 (Fig. 6a). Below ~ 300 μm from surface the hardness values are constant in each zone, differences are supposed to be evident due to the thermal treatment when manufacturing the wheel. An attempt to evaluate nanoindentation hardness (Fig. 6b) is done at various depths from surface, referring to the depths of the detailed SEM investigations. An increase in hardness can be seen within the outermost 100 μm from surface in all zones, however, scattering is very pronounced.

Various WEL-Like Microstructures on the Wheels

Various WEL-like microstructures are identified by etching the cross-sectional samples, with variations in appearance (bright shining to brownish), thicknesses (20–600 μm) as well as microstructure (Fig. 7).

The white appearing layer pictured in Fig. 7a is present on the tread surface in the region between zone 2 and 3. It comes up with a thickness of ~ 30 μm, formed top of an SPD aligned microstructure and numerous cracks origsnate within this layer (defined as WEL1 in this work). Figure 7b shows different WEL-like microstructures, more precisely a stratification of different layers. A large brownish appearing region extends down to 500 μm below the surface of zone 3. On top of this brownish region (defined as BEL) a brighter, more

homogenous and thinner layer is present, which is defined as WEL2. The combination can be designated as SSL. Some cracks stop at the interface of WEL2 and BEL, but at the margin of the SSL a crack propagates through both layers, arresting at the interface to the underlying microstructure. In some areas, the underlying material (below the SSL) is an SPD microstructure and in others an almost original coarse ferritic-pearlitic microstructure.

Detailed high-magnification SEM investigations of selected regions highlight the typical microstructure of the formed WEL-like microstructures (Fig. 7a and b). The thin and homogenous WEL1 has a uniform microstructure (Fig. 7c). Further increasing the magnification highlights a fine mesh-like structure with some evenly distributed sub-micron globular particles < 100 nm (Fig. 7d). The underlying SPD region exhibits a coarser and more aligned microstructure (Fig. 7e and f), corresponding to that presented earlier for a distance of ~ 50 μm below the wheel tread surface.

In general, WEL2 exhibits a comparable microstructure to WEL1 but the mesh-like structure tends to be demolished, compare Fig. 7c and d (WEL2) with Fig. 7g and h. Moreover, differences can be seen regarding hardness, where WEL1 reveals the highest values of 6.09 ± 0.43 GPa followed by WEL2 with 4.61 ± 0.46 GPa. The high-magnification SEM micrographs of the BEL (Fig. 7i and j) show a dissolved microstructure with spheroidized cementite and the hardness significantly decreased to 3.57 ± 0.50 GPa.

Discussion

When comparing individual studies about wear and fatigue phenomena of railway wheels, it is of utmost importance to know the loading history and whether there is a preferred
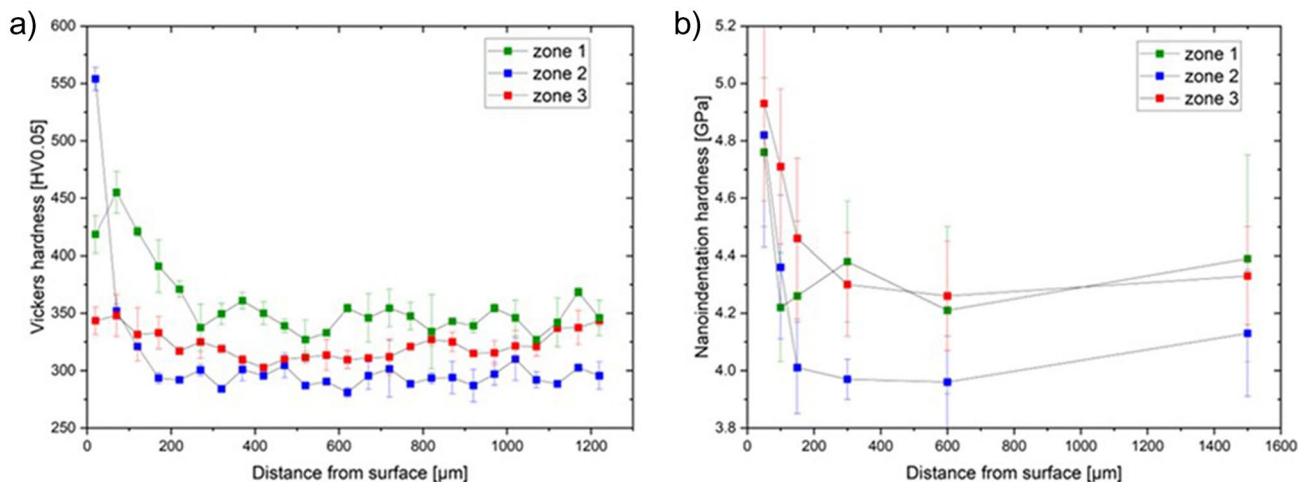

Fig. 6 Low-load Vickers hardness measurements (**a**) and nanoindentation hardness (**b**) graphs for the different zones
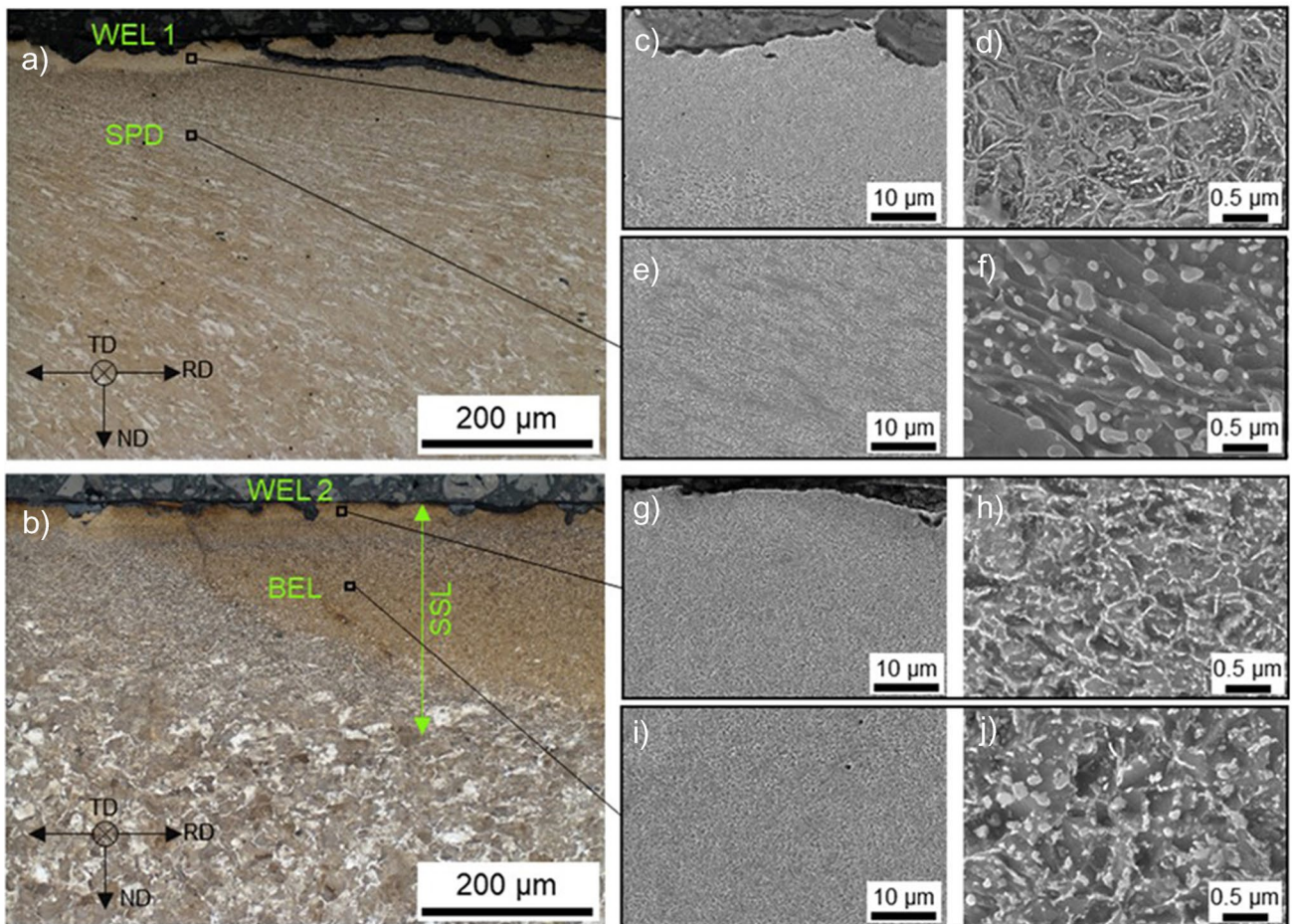
Fig. 7 (**a**) and (**b**) show overview micrographs of the investigated WEL-like microstructures. Detailed SEM investigations of the regions marked in (**a**) and (**b**) are presented in (**c**–**j**) with different magnifications: WEL1 (**c**) and (**d**), aligned SPD microstructure (**e**) and (**f**), WEL2 (**g**) and (**h**), and BEL (**i**) and (**j**)

rolling direction, or this changed periodically throughout the service like for the wheel studied in the current work. Whereas most of the studies focus on a certain zone along the railway wheel tread [43–45], we compared the microstructural evolution in the near-surface regions for different locations of the railway wheel tread. A corresponding study was conducted by Molyneux-Berry et al. [17] for a railway wheel being in service for ~280,000 km. For the region corresponding to our zone 1 (named region E in [17]) they report that there are few contacts (with the rail) but high tangential forces toward the middle of the tread, causing rolling contact fatigue (RCF) cracking. Our microstructural results are comparable (Fig. 2a and b, Fig. 3) exhibiting an about 300–500 μm deep deformed region with numerous small RCF cracks along the surface and some long but shallow cracks propagating toward the middle of the railway wheel tread. For this middle region, moderate normal stresses and circumferential tangential forces are present [17]. Due to various characteristics (e.g., traction, braking),

the peak loading tends to be in the near sub-surface region. Corresponding to the results reported in [17], our microstructural studies indicate a weaker line structure in transversal direction of this middle region (Fig. 2d) than for the cross section in rolling direction (Fig. 2c, Fig. 4). This–low shear strain values with minor deformed microstructure and practically featureless appearance for the middle sector of the railway wheel treat–is also reported by Cvetkovski and Ahlstrom [18]. Important to mention is also that for this middle region–being the main contact zone between wheel and rail–traction and breaking will lead to significant temperature influence on the railway wheel [17]. This thermal loading is sufficient to initiate spheroidization of broken cementite lamellae (due to the mechanical loading) [13, 16, 46], (Fig. 4a and b). Nikas et al. [9] studied different railway wheel materials and found comparable microstructures in this middle region of the railway wheel treat.

For the region of our zone 2, Molyneux-Berry et al. [17] proposed that significant normal and tangential stresses

lead to the formation of fine surface cracks, which tend to propagate not deep into the material. While in general, our microstructural observations are similar for this region, we do observe also cracks that propagate almost 500 μm deep into the material (Fig. 2e). This might be affected by the formation of a different WEL-like microstructures, which easily results in a different fracture toughness [1, 2, 4, 6, 7, 19, 20, 47, 48].

Corresponding detailed EBSD studies at different regions of the railway wheel to ours are so far mainly conducted for wheel materials loaded via a twin-disc setup [33, 49–60]. These lab-tests do have their advantages as the loading conditions are controlled, but a direct comparison of the thereby obtained microstructural changes with those present in railway wheels after service is difficult. Nevertheless, the deformation of ferrite and cementite lamella, their fragmentation and the subsequent formation of a sub-grain structure and fine-grained microstructure–as reported for materials tested with the twin disc setup [51] –was also observed for our wheel after service (Figs. 3, 4 and 5). Differences for our ex-service wheel are that in zone 1 an SPD microstructure with high GAM angles is present, resulting from high tangential forces [17] and that the fraction of small angle GB is higher for the measurement depth of 150 μm (Fig. 3g). Also for the other zones, 2 (Figs 3, 4g–j) and 3 (Fig. 5 g–j), the fraction of large angle GB is highest directly below the surface. The GAM is lowest in the middle region of the railway wheel treat (zone 3), where the highest thermal loading is present as discussed above, promoting dynamic recrystallization [52] and spheroidization of fragmented cementite lamellae. This leads to no significant hardness increase within zone 3 (Fig. 6a), in contrast to an increase for the other zones. Some studies measured an increase in hardness in the middle zone of an used rail wheel with values up to 300–400 HV1 [17, 61], however, the wheel grade and the loading history are different. In general, plastic deformed regions and fine-grained layers near the surface come up with hardness increases [51, 57] but due to local inhomogeneities of rail wheels from service the variation is large. This is also the issue for the presented nanoindentation measurement results (Fig. 6b), which were performed in the same depths as the detailed SEM investigations. A trend toward a hardness increase up to 5 GPa can be seen for all zones, but especially below 300 μm the coarse microstructure led to a large scattering of the nanoindentation results.

Our results clearly show the variety of WEL-like microstructures, whereby its formation depends on the different loading conditions present at the different zones of the railway wheel. Further, the initial local microstructure along the wheel tread potentially influences the formation [28]. Most characteristically the WEL-like microstructures lead to different colors during LOM investigations (Fig. 7a, b) and exhibit a different microstructure (during SEM investigations), as well as mechanical properties. The brightest WEL (WEL1 Fig. 7a, c, d) is thin and formed on top of an otherwise heavily deformed material, suggesting that short but intense slipping events are primarily responsible for their formation. A comparable microstructure and general appearance are reported by Handa et al. [11] for a wheel from service, and by Zhu et al. [50] for a wheel tested via a twin-disc setup with a 25% slip ratio. The large brownish (during LOM) appearing area (named here BEL, Fig. 7h) suggests a massive thermal influence (like present during heavy braking) because microstructural investigations after brake dynameter experiments yield a comparable result [11]. The microstructure is almost featureless with larger spheroidized cementite particles, which can be ascribed as BEL or tempered WEL, discussed in detail by Kumar et al. [35] for rails. Corresponding variations of WEL-like microstructures at the same location along the tread wheel surface are also reported by others [13, 32–34], but a different classification is still missing and most likely not meaningful due to the complex loading situation during service.

Conclusions

The near-surface regions of a railway wheel after almost 200,000 km in service exhibit huge variations in their microstructural evolution from the field side of the wheel treat to its flange, due to variations in loading situations.

The field side (named here zone 1) reveals numerous RCF cracks, indicative of high tangential forces toward the middle of the tread. A severe plastic deformed microstructure extends down to a depth of ~300 μm from the surface, with cementite fragmentation and even spheroidization. EBSD investigations show that the microstructure exhibits signs of deformation even down to 600 μm and a relatively high grain average misorientation. The corresponding hardness variation–which increases from the core value to the surface by only ~8%–is less pronounced than for the other zones along the surface tread. The microstructural changes in the region next to the wheel flange (named here zone 2) extend deeper into the material than for the field side. The microstructural features–like more pronounced elongation in rolling direction as well as alignment ~45° to the tread surface–indicate a comparably lower thermal loading history. The hardness at the surface is ~15% above the core value. The region between these, being the major tread surface (named here as zone 3), exhibits a microstructure with spheroidized cementite down to deeper regions as for the field side. This suggests that the thermal loading history was more severe. Furthermore, the region is characteristic of its fine-grained microstructure with minor preferred alignment,

low misorientation, and a higher fraction of large angle GBs near the surface.

In addition to these different microstructural evolutions and characteristics, variations of WEL-like microstructures are present, acting as potential crack initiation sites. The thin (~ 3 μm) and brightest appearing (after metallographic sample preparation) WEL (classified as WEL1) reveals a fine mesh-like structure and the highest hardness of 6.09 ± 0.43 GPa. The overall morphology of this WEL suggests a minor loading since formation, hence being relatively "young". This is in contrast to the other variation identified (classified as WEL2), which is up to 50 μm thick and exhibits a more flawed mesh-like microstructure suggesting severe loading since formation. This WEL appears more brownish-like during light optical microscopy and has a lower hardness with 4.61 ± 0.46 GPa. The third majorly different variation (classified as BEL) is softest (3.57 ± 0.50 GPa) and 500 μm thick. Its microstructure shows small spheroidized cementite particles and suggests even for their dissolution; hence, the ferrite would be supersaturated in C. Several reports indicate that such a BEL resulted from severe thermal loads generated during hard wheel braking and massive slippage events. The presented analysis shows the diversity of WEL-like microstructures in the field and can contribute to the knowledge of potential fatigue crack initiation sites. The highest tendency for crack-formation was found for the WEL1 and in its vicinity. Therefore, we classify WEL1 as more dangerous than WEL2 or BEL in terms of cracking risk. Knowledge of microstructural characteristics and mechanical properties, especially crack initiation and fracture behavior, is crucial for further improvement of railroad safety.

Conflict of interest On behalf of all authors, the corresponding author states that there is no conflict of interest.

References

1. X. Sauvage, A. Chbihi, X. Quelennec, Severe plastic deformation and phase transformations. J. Phys. Conf. Ser. **240**, 012003 (2010). https://doi.org/10.1088/1742-6596/240/1/012003
2. A. Ekberg, B. Åkesson, E. Kabo, Wheel/rail rolling contact fatigue–Probe, predict, prevent. Wear. **314**(1–2), 2–12 (2014). https://doi.org/10.1016/j.wear.2013.12.004
3. A. Ekberg, E. Kabo, H. Andersson, An engineering model for prediction of rolling contact fatigue of railway wheels. Fat. Frac. Eng. Mat. Struct. **25**(10), 899–909 (2002). https://doi.org/10.1046/j.1460-2695.2002.00535.x
4. J. Tunna, J. Sinclair, J. Perez, A review of wheel wear and rolling contact fatigue. Proc. Inst. Mech. Eng. Part F J. Rail Rapid Trans. **221**(2), 271–289 (2007). https://doi.org/10.1243/0954409JRRT72
5. A. Hohenwarter, A. Taylor, R. Stock, R. Pippan, Effect of large shear deformations on the fracture behavior of a fully pearlitic steel. Metall. Mat. Trans. A. **42**(6), 1609–1618 (2011). https://doi.org/10.1007/s11661-010-0541-7
6. S.J. Kwon, D.H. Lee, S.T. Kwon, B.C. Goo, Failure analysis of railway wheel tread. KEM. **321–323**, 649–653 (2006). https://doi.org/10.4028/www.scientific.net/KEM.321-323.649
7. F. Walther, D. Eifler, Fatigue behaviour of railway wheels at different temperatures: Interrelation of the microstructure and the fatigue behaviour of railway wheels at ambient and elevated temperatures. Mater. Test. **46**(4), 158–162 (2004). https://doi.org/10.3139/120.100576
8. M. Faccoli, A. Ghidini, A. Mazzù, Experimental and numerical investigation of the thermal effects on railway wheels for shoe-braked high-speed train applications. Metall. Mat. Trans. A. **49**(10), 4544–4554 (2018). https://doi.org/10.1007/s11661-018-4749-2
9. D. Nikas, J. Ahlström, A. Malakizadi, Mechanical properties and fatigue behaviour of railway wheel steels as influenced by mechanical and thermal loadings. Wear. **366–367**, 407–415 (2016). https://doi.org/10.1016/j.wear.2016.04.009
10. K. Knothe, S. Liebelt, Determination of temperatures for sliding contact with applications for wheel-rail systems. Wear. **189**(1–2), 91–99 (1995). https://doi.org/10.1016/0043-1648(95)06666-7
11. K. Handa, Y. Kimura, Y. Mishima, Ferrite and spheroidized cementite ultrafine microstructure formation in an Fe-0.67 Pct C steel for railway wheels under simulated service conditions. Metall. Mat. Trans. A. **40**(12), 2901–2908 (2009). https://doi.org/10.1007/s11661-009-0015-y
12. K.J. Sawley, Calculation of temperatures in a sliding wheel/rail system and implications for wheel steel development. Proc. Inst. Mech. Eng. Part F J. Rail Rapid Trans. **221**(4), 455–464 (2007). https://doi.org/10.1243/09544097JRRT120
13. J. Ahlstrom, B. Karlsson, Microstructural evaluation and interpretation of the mechanically and thermally affected zone under railway wheel flats. Wear. **232**(1), 1–4 (1999). https://doi.org/10.1016/S0043-1648(99)00166-0

14. M. Faccoli, A. Ghidini, A. Mazzù, Changes in the microstructure and mechanical properties of railway wheel steels as a result of the thermal load caused by shoe braking. Metall. Mat. Trans. A. **50**(4), 1701–1714 (2019). https://doi.org/10.1007/s11661-019-05135-x

15. O. Hajizad, A. Kumar, Z. Li, R.H. Petrov, J. Sietsma, R. Dollevoet, Influence of microstructure on mechanical properties of bainitic steels in railway applications. Metals. **9**(7), 778 (2019). https://doi.org/10.3390/met9070778

16. K. Cvetkovski, J. Ahlström, B. Karlsson, Thermal degradation of pearlitic steels: influence on mechanical properties including fatigue behaviour. Mater. Sci. Technol. **27**(3), 648–654 (2011). https://doi.org/10.1179/026708310X520538

17. P. Molyneux-Berry, C. Davis, A. Bevan, The influence of wheel/rail contact conditions on the microstructure and hardness of railway wheels. Sci. World J. (2014). https://doi.org/10.1155/2014/209752

18. K. Cvetkovski, J. Ahlström, Characterisation of plastic deformation and thermal softening of the surface layer of railway passenger wheel treads. Wear. **300**(1–2), 200–204 (2013). https://doi.org/10.1016/j.wear.2013.01.094

19. A. Al-Juboori et al., Characterisation of White Etching Layers formed on rails subjected to different traffic conditions. Wear. **436–437**, 202998 (2019). https://doi.org/10.1016/j.wear.2019.202998

20. M. Kerr, A. Wilson, S. Marich, 'The epidemology of squats and related rail defects', CORE 2008: Rail; the core of integrated transport: rail. Core Integr. Transp. Perth Railw. Tech. Soc. Australas. Eng. Aust. (2008). https://doi.org/10.3316/informit.564088292893778

21. J. Takahashi, K. Kawakami, M. Ueda, Atom probe tomography analysis of the white etching layer in a rail track surface. Acta Mater. **58**(10), 3602–3612 (2010). https://doi.org/10.1016/j.actamat.2010.02.030

22. J. Wu et al., Micro and nanoscale characterization of complex multilayer-structured white etching layer in rails. Metals. **8**(10), 749 (2018). https://doi.org/10.3390/met8100749

23. S.B. Newcomb, W.M. Stobbs, A transmission electron microscopy study of the white-etching layer on a rail head. Mater. Sci. Eng. **66**(2), 195–204 (1984). https://doi.org/10.1016/0025-5416(84)90180-0

24. G. Baumann, H.J. Fecht, S. Liebelt, Formation of white-etching layers on rail treads. Wear. **191**(1–2), 133–140 (1996). https://doi.org/10.1016/0043-1648(95)06733-7

25. W. Österle, H. Rooch, A. Pyzalla, L. Wang, Investigation of white etching layers on rails by optical microscopy, electron microscopy, X-ray and synchrotron X-ray diffraction. Mater. Sci. Eng., A. **303**(1–2), 150–157 (2001). https://doi.org/10.1016/S0921-5093(00)01842-6

26. H.W. Zhang, S. Ohsaki, S. Mitao, M. Ohnuma, K. Hono, Microstructural investigation of white etching layer on pearlite steel rail. Mater. Sci. Eng., A. **421**(1–2), 191–199 (2006). https://doi.org/10.1016/j.msea.2006.01.033

27. A. Al-Juboori et al., Squat formation and the occurrence of two distinct classes of white etching layer on the surface of rail steel. Int. J. Fatigue. **104**, 52–60 (2017). https://doi.org/10.1016/j.ijfatigue.2017.07.005

28. M. Freisinger et al., Comparative study on the influence of initial deformation and temperature of thermally induced white etching layers on rail wheels'. Tribol. Int. **177**, 107990 (2023). https://doi.org/10.1016/j.triboint.2022.107990

29. W. Lojkowski, M. Djahanbakhsh, G. Bürkle, S. Gierlotka, W. Zielinski, H.-J. Fecht, Nanostructure formation on the surface of railway tracks. Mater. Sci. Eng., A. **303**(1–2), 197–208 (2001). https://doi.org/10.1016/S0921-5093(00)01947-X

30. L. Wang, A. Pyzalla, W. Stadlbauer, E.A. Werner, Microstructure features on rolling surfaces of railway rails subjected to heavy loading. Mater. Sci. Eng., A. **359**(1–2), 31–43 (2003). https://doi.org/10.1016/S0921-5093(03)00327-7

31. A. Pyzalla, L. Wang, E. Wild, T. Wroblewski, Changes in microstructure, texture and residual stresses on the surface of a rail resulting from friction and wear. Wear. **251**(1–12), 901–907 (2001). https://doi.org/10.1016/S0043-1648(01)00748-7

32. R. Lewis et al., Mapping railway wheel material wear mechanisms and transitions. Proc. Inst. Mech. Eng. Part F J. Rail Rapid Trans. **224**(3), 125–137 (2010). https://doi.org/10.1243/09544097JRRT328

33. D. Zeng, L. Lu, Y. Gong, Y. Zhang, J. Zhang, Influence of solid solution strengthening on spalling behavior of railway wheel steel. Wear. **372–373**, 158–168 (2017). https://doi.org/10.1016/j.wear.2016.12.025

34. J. Jergéus, C. Odenmarck, R. Lundén, P. Sotkovszki, B. Karlsson, P. Gullers, Full-scale railway wheel flat experiments. Proc. Inst. Mech. Eng. Part F J. Rail Rapid. Trans. **213**(1), 1–13 (1999). https://doi.org/10.1243/0954409991530985

35. A. Kumar, G. Agarwal, R. Petrov, S. Goto, J. Sietsma, M. Herbig, Microstructural evolution of white and brown etching layers in pearlitic rail steels. Acta Mater. **171**, 48–64 (2019). https://doi.org/10.1016/j.actamat.2019.04.012

36. S. Li, J. Wu, R.H. Petrov, Z. Li, R. Dollevoet, J. Sietsma, Brown etching layer: a possible new insight into the crack initiation of rolling contact fatigue in rail steels? Eng. Fail. Anal. **66**, 8–18 (2016). https://doi.org/10.1016/j.engfailanal.2016.03.019

37. M. Messaadi, M. Steenbergen, Stratified surface layers on rails. Wear. **414–415**, 151–162 (2018). https://doi.org/10.1016/j.wear.2018.07.019

38. P.-Y. Tung, X. Zhou, L. Morsdorf, M. Herbig, Formation mechanism of brown etching layers in pearlitic rail steel. Materialia. **26**, 101625 (2022). https://doi.org/10.1016/j.mtla.2022.101625

39. 'EN 13262:2004+A2:2011: Railway applications - Wheelsets and bogies-Wheels-Product requirements

40. M. Diener, A. Ghidini, Fracture toughness: a quality index for railway solid wheels. Matls. Perf. Charact. **3**(3), 20130047 (2014). https://doi.org/10.1520/MPC20130047

41. R. Deuce, Wheel tread damage-an elementary guide, Bombardier Transportation GmbH, Netphen, Germany, Technical Report, (2007)

42. W.C. Oliver, G.M. Pharr, An improved technique for determining hardness and elastic modulus using load and displacement sensing indentation experiments. J. Mater. Res. **7**(6), 1564–1583 (1992). https://doi.org/10.1557/JMR.1992.1564

43. J. Dearden, The wear of steel rails and tyres in railway service. Wear. **3**(1), 43–59 (1960). https://doi.org/10.1016/0043-1648(60)90174-5

44. Z. Ławrynowicz, Plastic deformation and softening of the surface layer of railway wheel. Adv. Mater. Sci. **15**(4), 5–13 (2015). https://doi.org/10.1515/adms-2015-0018

45. B. Gao et al., Influence of non-uniform microstructure on rolling contact fatigue behavior of high-speed wheel steels. Eng. Fail. Anal. **100**, 485–491 (2019). https://doi.org/10.1016/j.engfailanal.2019.03.002

46. T. Vernersson, S. Caprioli, E. Kabo, H. Hansson, A. Ekberg, Wheel tread damage: a numerical study of railway wheel tread plasticity under thermomechanical loading. Proc. Inst. Mech. Eng. Part F J. Rail Rapid Trans. **224**(5), 435–443 (2010). https://doi.org/10.1243/09544097JRRT358

47. A. Kumar et al., In situ study on fracture behaviour of white etching layers formed on rails. Acta Mater. **180**, 60–72 (2019). https://doi.org/10.1016/j.actamat.2019.08.060

48. M. Freisinger, L. Zauner, R. Hahn, H. Riedl, P.H. Mayrhofer, In-situ micro-cantilever bending studies of a white etching layer thermally induced on rail wheels. Mater. Sci. Eng. A. **869**, 144805 (2023). https://doi.org/10.1016/j.msea.2023.144805

49. Y. Zhou, J.F. Peng, W.J. Wang, X.S. Jin, M.H. Zhu, Slippage effect on rolling contact wear and damage behavior of pearlitic steels. Wear. **362–363**, 78–86 (2016). https://doi.org/10.1016/j.wear.2016.05.001

50. W.T. Zhu et al., Wear and damage transitions of two kinds of wheel materials in the rolling-sliding contact. Wear. **398–399**, 79–89 (2018). https://doi.org/10.1016/j.wear.2017.11.023

51. C.G. He et al., On the microstructure evolution and nanocrystalline formation of pearlitic wheel material in a rolling-sliding contact. Mater. Charact. **164**, 110333 (2020). https://doi.org/10.1016/j.matchar.2020.110333

52. Y. Hu et al., Microstructure evolution of railway pearlitic wheel steels under rolling-sliding contact loading. Tribol. Int. **154**, 106685 (2021). https://doi.org/10.1016/j.triboint.2020.106685

53. J. Hua, X. Zhao, P. Liu, J. Pan, C. Su, R. Ren, Study on the mechanism for polygonisation formation of D2 wheel steel and its effect on microstructure and properties under rolling wear conditions. Wear. **450–451**, 203261 (2020). https://doi.org/10.1016/j.wear.2020.203261

54. Y. Hu et al., Effect of rolling direction on microstructure evolution of CL60 wheel steel. Wear. **424–425**, 203–215 (2019). https://doi.org/10.1016/j.wear.2019.02.022

55. J. Hua et al., EBSD Study on proeutectoid ferrite and eutectoid ferrite refinement mechanism of D2 wheel steel under a rolling condition. Tribol. Lett. **69**(4), 148 (2021). https://doi.org/10.1007/s11249-021-01527-6

56. C. Liu, R. Ren, D. Liu, X. Zhao, C. Chen, An EBSD investigation on the evolution of the surface microstructure of D2 wheel steel during rolling contact fatigue. Tribol. Lett. **68**(1), 47 (2020). https://doi.org/10.1007/s11249-020-1277-1

57. L. Ma et al., Study on wear and rolling contact fatigue behaviors of wheel/rail materials under different slip ratio conditions. Wear. **366–367**, 13–26 (2016). https://doi.org/10.1016/j.wear.2016.04.028

58. G. Donzella, M. Faccoli, A. Mazzù, C. Petrogalli, R. Roberti, Progressive damage assessment in the near-surface layer of railway wheel–rail couple under cyclic contact. Wear. **271**(1–2), 408–416 (2011). https://doi.org/10.1016/j.wear.2010.10.042

59. C.G. He et al., Experimental investigation on the effect of tangential force on wear and rolling contact fatigue behaviors of wheel material. Tribol. Int. **92**, 307–316 (2015). https://doi.org/10.1016/j.triboint.2015.07.012

60. T. Kato, Effect of elevated temperature on shelling property of railway wheel steel. Wear. **266–267**, 359–367 (2016). https://doi.org/10.1016/j.wear.2016.04.015

61. D.F.C. Peixoto, P.M.S.T. de Castro, Fatigue crack growth of a railway wheel. Eng. Fail. Anal. **82**, 420–434 (2017). https://doi.org/10.1016/j.engfailanal.2017.07.036